

Spontaneous symmetry breaking in transition metal oxides

THÈSE

*présentée à la Faculté des Sciences de l'Université de Genève
pour obtenir le grade de docteur ès Sciences, mention Physique*

par

Adrien Stucky

de
Genève (Suisse)

Thèse n° 00000

GENÈVE
Imprimerie HARDER
2016

Contents

1	Quest of the Higgs mode	1
1.1	Higgs mechanism	2
1.1.1	Reconsideration of the notion of the mass	2
1.1.2	The problem of the gauge bosons masses	2
1.1.3	Higgs and Goldstone modes in condensed matter physics	4
1.2	Hexagonal manganites	5
1.2.1	Crystal structure	5
1.2.2	Multiferroicity	6
1.2.3	Ferroelectric domains and trimerization	9
1.3	Optical spectroscopy investigation	14
1.3.1	State of the art	14
1.3.2	Theoretical expectations for the Higgs and Goldstone modes	15
1.3.3	Samples	16
1.3.4	Raman spectroscopy	16
1.4	Discussion	20
1.5	Conclusion	21
	Accepted and submitted Papers	23
	References	25

CHAPTER 1

Quest of the Higgs mode

*Every person takes the limits of their own field
of vision for the limits of the world.*

Arthur Schopenhauer

Drawing connections between apparently disconnected domains of modern physics is a rare and exciting opportunity. This chapter has the very interesting aspect of building an analogy between the Higgs mechanism of quantum field theory and an optical active mode existing in some multiferroic compounds. Thus, the optical spectroscopy in condensed matter physics transforms into a measuring tool for exploring the spontaneous symmetry breaking in particle physics. In this chapter, two types of hexagonal manganites (ErMnO_3 and InMnO_3) are investigated by optical spectroscopy with the aim of finding a Higgs mode. This work is done in collaboration with the group of Material theory of Prof. Nicola Spaldin.

1.1 Higgs mechanism

In particle physics, the Higgs mechanism allows to reconsiderate the origin of the mass of elementary particles. Developed to account for explaining the unexpected non-zero mass of the gauge bosons of the weak interaction, it consists of a model which relies on the spontaneous symmetry breaking. Interestingly, it can also be applied to some specific fields of condensed matter physics which will be presented later.

1.1.1 Reconsideration of the notion of the mass

Let us begin with a very simple question: *What is the mass?*. Although it might appear as a trivial interrogation, the fundamental answer to this question is still a work in progress. The concept of mass has the particularity to have constantly evolved from the beginning of the modern science until now. The fact that the inertial mass (appearing in second Newton's law) was the same as the gravitational mass was a curiosity that was not fully explained until the theory of general relativity.

In the beginning of the 20th century, the relation between mass and motion was extended to a relation between mass and energy. The mass–energy equivalence was first evoked by *H. Poincaré* and rapidly re-formulated by *A. Einstein* in 1905 as the consequence of the invariability of the speed of light and the equivalence principle. The formula $E_0 = mc^2$, taken as effigy for the modern physics, revolutionized the idea of mass.

Since the discovery of the Higgs bosons at CERN in 2012 [1], the accepted definition of the mass for non-specialists has somehow changed. The mass is then understood as the interaction between the fundamental particles and a complex scalar field whose quanta is the Higgs boson. An interesting analogy invented to democratize the idea of the Higgs boson was made by J. Ellis [2]. The complex scalar field is represented by the snowpack where each snowflake is a Higgs boson forming a fundamental snow scalar field. The motion of an object through the snow depends on its interaction with the object and the white field. A light particle could be seen as a skier with a very modern material while a heavy particle is associated to a snowshoeing person.

1.1.2 The problem of the gauge bosons masses

The reconsideration of the mass was born from one of the most important problem of the particle physics in the fifties ; the inability to explain the non-zero mass of gauge bosons of the weak interaction. The gauge invariance in field theory imposes by rules of breaking symmetry that the gauge bosons are massless. According to the

Goldstone theorem: "If there is continuous symmetry transformation. . . then either the vacuum state is invariant under the transformation or there must exist spinless particles of zero mass." [3]. However since 1983, the three intermediate vector bosons (Z , W^+ and W^-) have a mass estimate that is ten times heavier than the electron [4],[5]. The most recent estimation of their masses gives: $m_Z = 91.18$ [GeV/c^2] and $m_W = 80.39$ [GeV/c^2] [6].

The theoretical model of particle physics was then incomplete and at a loss to explain the mass of these three bosons. Indeed, the mechanism of superconductivity of material has promoted some very important model of spontaneous symmetry breaking. The BCS theory is still used to explain the superconducting mechanism in conventional superconductors. This model is presented in Sec. ???. Nambu discussed a resolution of this problem by analyzing the Goldstone proposal in the spontaneous symmetry breaking system for quasi-particle and gauge invariance in the theory of superconductivity [7]. In fact, Nambu was studying the spontaneous symmetry breaking in BCS theory and found that a specific boson was created through a specific means. This massless and spinless boson (called Goldstone boson) gave the mass to the other boson in the system. In the following time, Anderson established the structure of such a mechanism in the BCS model [8].

At the same time the mechanism of Nambu-Anderson was adapted to particle physics theory in the same time by three different groups in 1964 [9–11]. The new suggestion was the following: when a gauge theory is combined with an additional field that spontaneously breaks the symmetry group, the gauge bosons can consistently acquire a nonzero mass. The introduction of the Higgs mechanism in particle physics gave rise to the Standard Model as it is known today. F. Englert and P. W. Higgs received the Nobel Prize in 2013 after the experimental discovery of the Higgs boson in 2012 [1].

The simplest form for a free-energy surface when a complex scalar field $\Psi = |\Psi| e^{i\phi}$ acquires a nonzero value and the field energy has a minimum away from zero [12] is expressed as a function of the amplitude z and the azimuthal angle ϕ as:

$$V(|\Psi|, \phi) = \lambda \left(|\Psi|^2 - \Psi_0^2 \right)^2 \quad (1.1)$$

where λ and Ψ_0 are model parameters. Fig. 1.1 presents a schematic representation of the free energy surface of the Eq. 1.1. The plot of this potential has a Mexican hat shape. One should note that the potential has a minimum not in $|\Psi| = 0$ but in a ditch independent of ϕ at fixed $|\Psi|$.

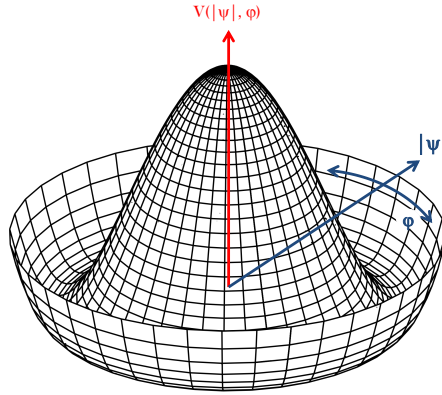


Figure 1.1: Schematic Mexican hat potential inspired by [13].

1.1.3 Higgs and Goldstone modes in condensed matter physics

Spontaneous symmetry breaking in crystals lead to a free-energy surface such as the Mexican hat in the Higgs model. Considering this Mexican hat shape of the free-energy surface for the complex scalar field, two oscillating modes can be defined. The Higgs mode corresponds to the oscillation in the rime of the Mexican hat with a fixed phase and an oscillating amplitude $|\psi|$. On the contrary, the Goldstone mode oscillates in the rime with a fixed value of the amplitude and an oscillating value of the phase.

A direct analogy is then done with a crystalline system where a spontaneous symmetry breaking induces a Mexican hat free-energy surface. Note that a Goldstone mode has already been observed in TlCuCl_3 [14–16]. In this material, the analysis of the magnetic excitations in the ordered regimes led to the observation of a mode corresponding to the phase fluctuations of the ordered moment. This mode was then associated by analogy to a Goldstone mode. To my best knowledge, a direct relation between an active mode in a material and a Higgs mode has not been established yet. A structural spontaneous symmetry breaking in a crystal leads to a Mexican hat-type surface of the free-energy, where the created boson is a phononic mode. The optical study of crystals with this kind of structural spontaneous symmetry breaking then allows to associate a phonon to a Higgs mode.

1.2 Hexagonal manganites

1.2.1 Crystal structure

The hexagonal manganites belong to a hexagonal space group with a general chemical formula $R\text{-MnO}_3$ where R denotes a small radius rare earth ion that can be: Dy, Ho, Er, Tm, Yb, Lu, Y or Sc. Indium can also take the place of the rare earth ion. In this type of structure, the small radius of the ion induces a hybridization state of the manganese Mn^{3+} leading to an oxygen repartition around it on the corners of a double tetrahedron. This type of structure is different from the cubic perovskite where a bigger size of the ion induced a hybridization of the manganese Mn^{4+} with an repartition of the oxygen atoms on a octahedron. A structural spontaneous symmetry breaking is observed in the hexagonal manganites leading to a Mexican hat-type free-energy surface. This kind of materials are then useful for the Higgs mode investigation. Fig. 1.2 shows the representation of the crystal structure. It consists of a perovskite structure with corner-sharing MnO_5 trigonal bi-pyramids forming triangular layers separated by layers of R ions [17]. At high-temperature, the system finds its minimum potential energy in the centro-symmetric space group of $P6_3mmc$, while at room temperature, the crystal symmetry is in the $P6_3cm$ space group. Fig. 1.2 shows the crystal structure of the hexagonal manganite at room temperature. In the $P6_3cm$ symmetry the bi-pyramids have a triangular base of nonequivalent oxygen sites and the elementary cell contains six formula units.

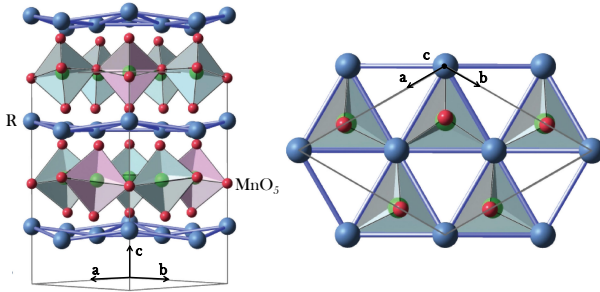


Figure 1.2: Two different views of the crystal structure of hexagonal rare earth manganites [18].

Two types of hexagonal manganites are considered in this thesis: ErMnO_3 and InMnO_3 . In the hexagonal $P6_3cm$ symmetry, these compounds have the following lattices parameters:

$$\begin{aligned} \text{ErMnO}_3 : a &= 6.112 \text{ \AA} & c &= 11.40 \text{ \AA} & \gamma &= 120^\circ \text{ [19]} \\ \text{InMnO}_3 : a &= 5.876 \text{ \AA} & c &= 11.47 \text{ \AA} & \gamma &= 120^\circ \text{ [20]} \end{aligned}$$

1.2.2 Multiferroicity

The hexagonal manganites are multiferroics of type I with a geometric mechanism. This kind of scenario is presented in Sec. ???. The magnetic property arises from the manganese atoms whereas the ferroelectricity is induced by the tilts of the rigid MnO_5 double tetrahedron.

The hexagonal manganites are paramagnetic at room temperature. The magnetic susceptibility measurement as a function of the temperature on ErMnO_3 , respectively on InMnO_3 , leads to the observation of a Néel temperature at 80K [21], respectively at 100K [20]. The left panels of Fig. 1.3 show the (a) magnetic susceptibility, (b) the dielectric constant and (c) the heat capacity of ErMnO_3 as a function of temperature. The right panels of Fig. 1.3 show the magnetic susceptibility of InMnO_3 as a function of two different temperature ranges for InMnO_3 .

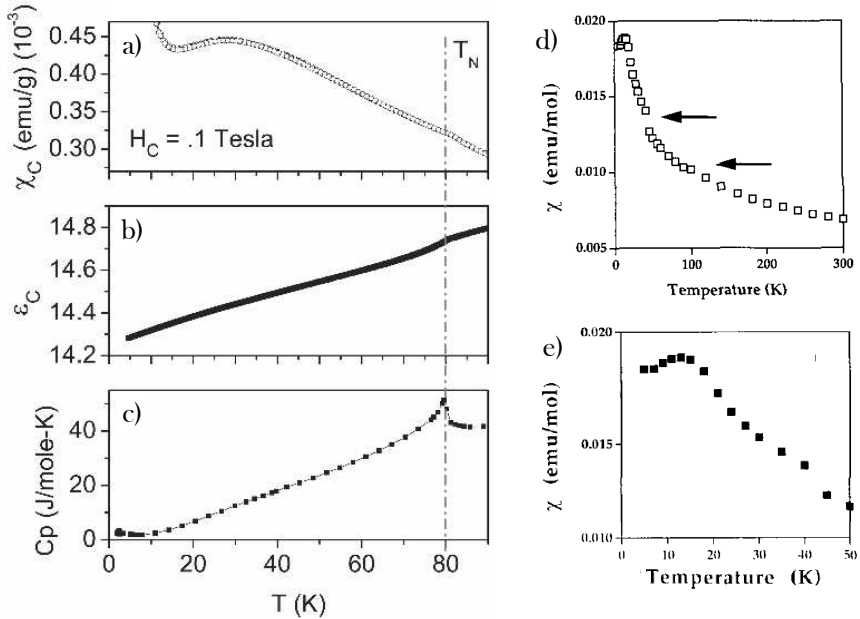


Figure 1.3: (a) Magnetic susceptibility along the c axis, (b) dielectric constant curve along the c axis at 1 kHz and (c) heat capacity as a function of temperature for ErMnO_3 [21]. (d) Magnetic susceptibility as a function of temperature for InMnO_3 (e) zoom at low temperature [20].

The magnetic order occurring at the phase transition between the paramagnetic and the anti-ferromagnetic order in hexagonal manganite is related to the triangular

sub-lattice of the Mn^{3+} ions. The two triangular sublattices are represented in Fig. 1.4 in blue and red color. The primary interaction between the Mn magnetic moments in this triangular lattice is an antiferromagnetic super-exchange inducing a frustrated ground state [19, 22]. This frustration is resolved by the spins forming a 120° noncollinear arrangement with the spins lying in the plane. There are then two possible arrangements of spin orientation between the two layers. Fig. 1.4(a) shows the first possible spin arrangement where the pairs of Mn spins are parallel while Fig. 1.4(b) presents the second arrangement where the pairs are antiparallel.

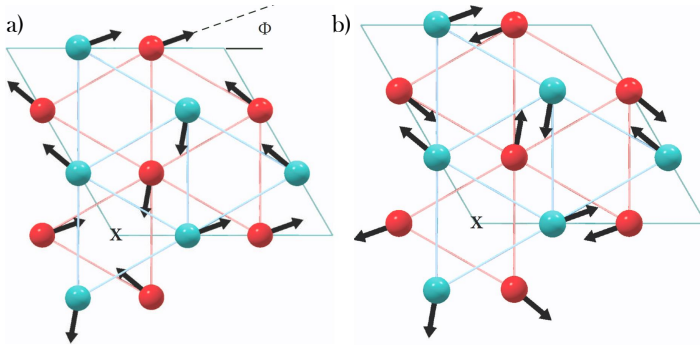


Figure 1.4: Triangular sublattices of Mn ions of hexagonal manganites in the ab plane. The two sublattices of Mn atoms are distinguished by the colors blue and red. The two possible spin arrangements are (a) parallel and (b) antiparallel [18].

It is interesting to note that the hexagonal manganites do not fulfill the conventional conditions of the ferroelectricity. Indeed, the hexagonal manganites possess neither an ion with an empty d orbital ("Matthias rule") nor a lone pair of electrons. In the case of YMnO_3 , it was previously proposed that the ferroelectricity was induced by the off-centering of the Mn atoms in the center of the oxygen cage [17]. Recently, Van Aken *et al.* proposed a new mechanism of ferroelectricity in YMnO_3 based on the tilt of the double tetrahedron [23]. They proved, with high resolution X-Ray diffraction combined with DFT calculations, that the Mn atoms do not move in the octahedron. Fig. 1.5(a) shows the centro-symmetric paraelectric phase occurring at high temperature where the Y layer, parallel to the ab plane, is flat and the octahedrons are aligned. Fig. 1.5(b) shows the scenario of the ferroelectric phase where the mirror plane perpendicular to the hexagonal c axis is lost and the double tetrahedrons are no more aligned.

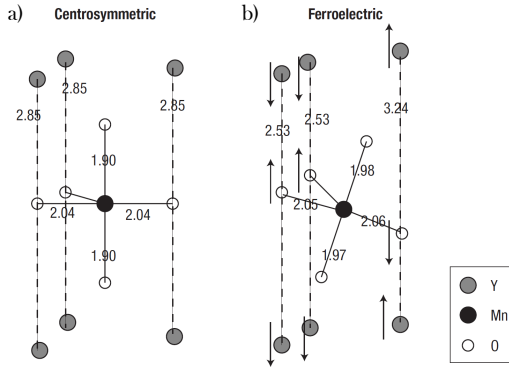


Figure 1.5: The atomic positions calculated by DFT: (a) high temperature centrosymmetric paraelectric phase and (b) ferroelectric phase. The numbers give the bond lengths in Å and the arrows indicate atomic displacements with respect to the centro-symmetric structure [23]

This scenario proposes that long-range dipole–dipole interactions combined to the double tetrahedrons rotations cooperate to drive the system towards the stable ferroelectric state. The polarization is then a direct consequence of the unusual Y-site coordination. In this thesis, it was assumed that this model applied to the case of ErMnO_3 . In contrast, a different non-ferroelectric ground-state structure is considered for InMnO_3 .

An additional centro-symmetric $P\bar{3}c$ phase is proposed as the ground-state structure by Kumagai *et al.* in [24]. Fig. 1.6 shows the crystal structure of the two different phases of InMnO_3 . Fig. 1.6(a) shows the side view of the $P6_3cm$ ferroelectric phase while Fig. 1.6(b) shows the side view of the new proposed non-ferroelectric $P\bar{3}c$ phase. The arrows on the In site indicate the displacements from the high-symmetry paraelectric $P6_3/mcm$ phase related to the tilts of the octaedron and thus, to the ferroelectricity. Note that, in the unit cell of the $P\bar{3}c1$ space group, an In ion remains at the high-symmetry site, retaining the inversion symmetry. Moreover, some different tilt patterns of the MnO_5 double tetrahedrons toward or around corner R ions are observed.

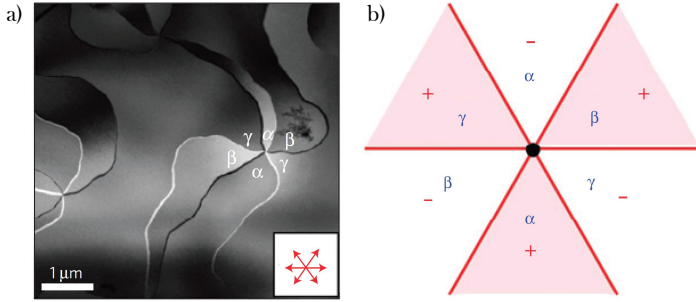


Figure 1.7: (a) TEM dark-field image showing six anti-phase domains emerging from one central point. The red arrows in the insets indicate anticipated crystallographic directions of anti-phase boundaries. (b) Configuration proposed for the cloverleaf domains [26].

Fig. 1.8 shows the three stable scenarios according to the spatial arrangement of the MnO_5 double tetrahedrons. Indeed, in the low-symmetry $P6_3cm$ ferroelectric phase, the MnO_5 double tetrahedrons find a minimum energy along three different tilt orientations. The orientation of the tilt is parametrized by the angle Φ defined in Fig. 1.8 as (a) 0, (b) $\pi/3$ and (c) $2\pi/3$. The trimerization phases $\Phi = 0, \pi/3, 2\pi/3$ correspond to the state $\alpha^+, \gamma^-, \beta^+$.

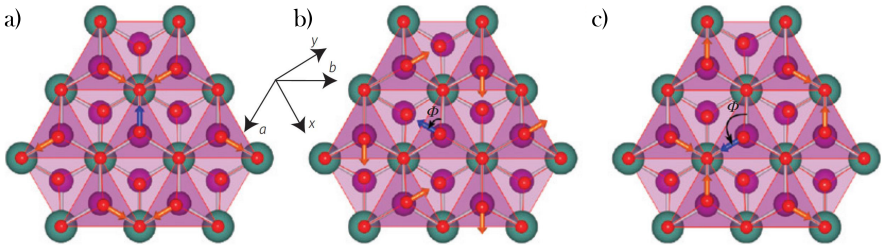


Figure 1.8: Crystal structure of hexagonal manganites projected on the ab plane. The red spheres, respectively purple and green, represent the oxygen atoms, respectively the manganese atoms and the cation ions. The arrows indicate the projections of the displacements of apical oxygen ions in the trimerized state. One ion (blue arrow) is chosen to define the trimerization phase Φ with (a) $\Phi=0$, (b) $\Phi=\pi/3$ and (c) $\Phi=2\pi/3$ [28].

Moreover, each tilt orientation can be "in" or "out" depending on the position of the R ions in the structure. Fig. 1.9 shows the two possible degenerated states where the left schema represents the "out" state while the right one shows the "in" state. The blue arrow on the cation ion represents the displacement from the high-symmetry phase and is related to the spontaneous polarization P .

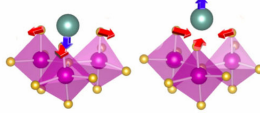


Figure 1.9: Schema of three neighbouring MnO_5 double tetrahedrons according to the "in" and "out" tilt orientation [29].

According to the periodic lattice modulation in a layered system, the trimerization is described entirely by the spatial amplitude Q between the vertical axis and the tilted angle and the phase Φ . Note that physically, Φ is the azimuthal angle describing the in-plane displacements of apical oxygen.

By considering the transformation properties of the trimerization phase Φ and the polarization \mathcal{P} , the Landau free-energy is written in power of Q , Φ and \mathcal{P} as:

$$\begin{aligned}
 f = & \frac{a}{2}Q^2 + \frac{b}{4}Q^4 + \frac{Q^6}{6} (c + c' \cos 6\Phi) \\
 & - gQ^3\mathcal{P} \cos 3\Phi + \frac{g'}{2}Q^2\mathcal{P}^2 + \frac{a_{\mathcal{P}}}{2}\mathcal{P}^2 \\
 & + \frac{1}{2} \sum_{i=x,y,z} [s_Q^i (\partial_i Q \partial_i Q + Q^2 \partial_i \Phi \partial_i \Phi) + s_Q^i \partial_i \mathcal{P} \partial_i \mathcal{P}]
 \end{aligned} \tag{1.2}$$

where \mathcal{P} is the amplitude of the zone-center mode proportional to the polarization, and the model parameters ($a, b, c, c', g, g', a_{\mathcal{P}}, s_{Q,\mathcal{P}}^i$) are calculated in [28]. Fig. 1.10 shows the contour plot of the free energy obtained by *ab initio* calculations and expressed as a function of the two trimerization parameters Q and Φ . Note that in this plot the polarization \mathcal{P} has been optimized for each Q and Φ .

The trimerization in hexagonal manganite due to the spontaneous symmetry breaking of the $P6_3cm$ ferroelectric phase leads to a free-energy surface which is analogous to the Mexican hat potential. Indeed, the minimum energy is not in (0,0), but localized in the rime of the Mexican hat. The six minima correspond to six "pockets" in the rime, each being associated to one of the six ferroelectric states observed in the cloverleaf pattern.

For the case of InMnO_3 in the partially undistorted anti-polar (PUA) phase with the $P\bar{3}c1$ symmetry, some new anti-polar states have been observed. Indeed, the non-ferroelectric phase induces 6 new angles of MnO_5 tilting [30]. In fact, PUA state presents some PUA vortices analogous to those in the FE. Concretely, the $P\bar{3}c1$ phase is obtained from the high-temperature $P6_3mmc$ prototype by tilting of the MnO_5 double tetrahedrons at intermediate angles. Fig. 1.11(a) shows the TEM image of InMnO_3 in the ferroelectric state with the cloverleaf pattern introduced previously

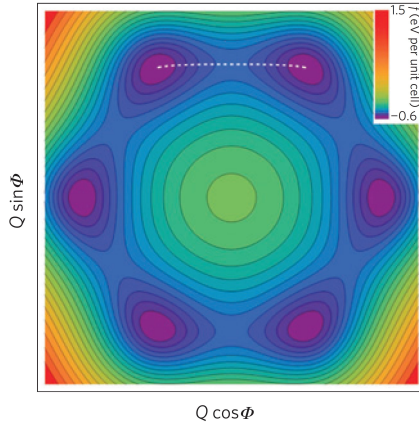


Figure 1.10: Contour plot of the free energy of uniformly trimerized states as a function of Q and Φ . The trajectory $Q(\Phi)$ (white dashed line) connecting two neighboring energy minima corresponds to the lowest-energy structural domain wall. [28]

while Fig. 1.11(b) shows the TEM image of InMnO_3 in the PUA state with a analog cloverleaf pattern.

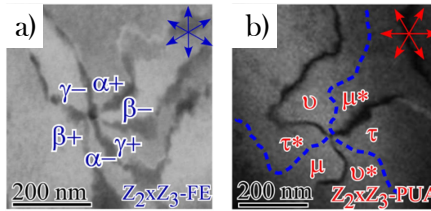


Figure 1.11: (a) A superlattice DF-TEM image showing a ferroelectric vortex in InMnO_3 in the $P6_3cm$ symmetry. (b) A superlattice DF-TEM image showing a PUA vortex in InMnO_3 in the $P\bar{3}c1$ symmetry [30].

The $P6_3mmc$ symmetry then leads to 12 degenerate states composed by 6 ferroelectric and 6 PUA states. The middle panel of Fig. 1.12 shows the representation of the 12 degenerated states of the $P6_3mmc$ symmetry. The 6 ferroelectric states on the left side of the figure have to be compared to the 6 PUA states presented on the right side.

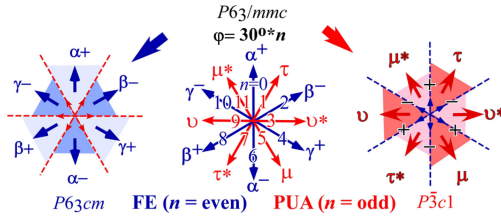


Figure 1.12: Representation of the 12 degenerated states of the $P6_3mmc$ symmetry. On the left side, the six ferroelectric state of $P6_3cm$ symmetry and on the right side the six PUA states observed in $P\bar{3}c1$ symmetry.[30].

The same approach which leads to the establishment of the free-energy surface with a Mexican hat shape is used for the spontaneous symmetry breaking of the $P6_3mmc$ in the $P\bar{3}c1$ symmetry. Fig. 1.13 shows the resulting Mexican hat shape for the two phases of InMnO_3 . The free-energy surface has a shape which is analogous to the mexican hat one but which is tilted by an angle of $\pi/6$.

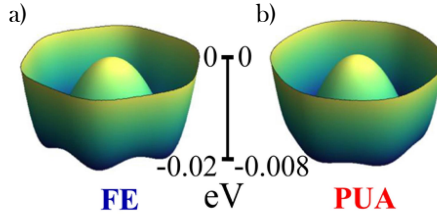


Figure 1.13: Calculated Mexican hat-shape energy landscapes for FE (left) and PUA (right) in InMnO_3 [30].

By definition, in the Mexican hat free-energy surface obtained by the spontaneous symmetry breaking, the Higgs mode then corresponds to the oscillation of the amplitude Q at constant Φ in the six minimums of the Mexican hat free-energy surface, while the Goldstone mode is related to the oscillation in Φ at constant Q . Optical spectroscopy is one of the most direct tools to observe this phonon.

1.3 Optical spectroscopy investigation

1.3.1 State of the art

The factor group analysis for the Γ -point phonon modes of hexagonal manganite $P6_3cm$ leads to the consideration of 60 modes [31].

$$\Gamma = 10A_1 + 5A_2 + 10B_1 + 5B_2 + 15E_1 + 15E_2 \quad (1.3)$$

where 38 modes ($9A_1 + 14E_1 + 15E_2$) are Raman active and 23 ($9A_1 + 14E_1$) are infrared actives [32]. Note that according to the geometric properties, only the A_1 mode are active in Raman spectroscopy if a transverse polarized light is used.

Very few optical analysis have been done on ErMnO_3 and InMnO_3 . This is partially due to difficulties to grow large size single crystal of hexagonal manganite. A Raman spectroscopy analysis was performed by Vermette *et al.* on ErMnO_3 with polarized light[33]. Fig. 1.14 shows the Raman scattering as a function of the Raman shift and temperature. The predicted extinction of the A_1 modes is observed by comparing the Raman spectroscopy in the two (parallel and perpendicular) configurations.

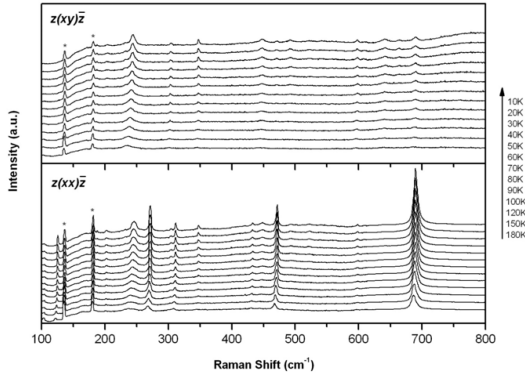


Figure 1.14: Raman spectroscopy of ErMnO_3 as a function of temperature with two configuration polarizations. Upper panel: perpendicular polarization and lower panel: parallel configuration. The stars indicate satellite peaks related to the beam source. [33]

A characterization of a single crystal of InMnO_3 was performed with Raman spectroscopy by Berkheet *et al.* in order to probe the $P6_3cm$ symmetry. Fig. 1.15 shows the Raman scattering as a function of the Raman shift for various temperatures ranging from room temperature up to 600°C . The $P6_3cm$ phase is found stable until 600°C but the ratio signal/noise of the spectrum is very weak. In spite of that, this

measurement indicates that the polar non-centrosymmetric structure of InMnO_3 is stable until 600°C .

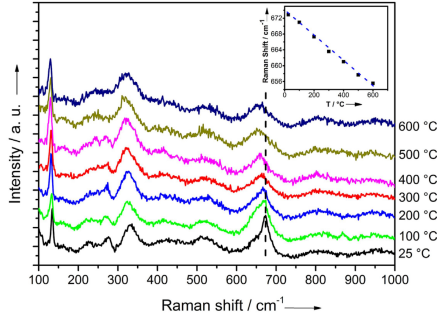


Figure 1.15: Raman spectra of InMnO_3 single crystal in the $P6_3cm$ with the symmetry. Curves are shifted on the vertical axis as a function of the temperature. The inset shows the linear decrease of the Raman shift of the 673 cm^{-1} mode band as a function of the temperature [34].

A more precise study in the Raman spectroscopy was then necessary to be performed in ErMnO_3 and InMnO_3 in the $P6_3cm$ as a function of temperature in order to probe the Higgs mode. Moreover, the optical study of InMnO_3 in the $P3c1$ phase has yet to be done.

1.3.2 Theoretical expectations for the Higgs and Goldstone modes

The expression of the Landau free-energy (Eq. 1.2) allows the determination of the frequency of the Higgs and the Goldstone modes for the three different samples. The theoretical expected frequencies are provided by the group of Prof. N. A. Spaldin [35] and are reported in the Tab. 1.1

Modes	ErMnO_3 FE	InMnO_3 PUA	InMnO_3 FE
Goldstone (cm^{-1})	107.4		87.5
Higgs (cm^{-1})	130.3	138.3	139.4

Table 1.1: Theoretical frequencies of the Goldstone and the Higgs modes for the three samples

1.3.3 Samples

Three hexagonal manganite single crystals grown by F. Lichtenberg from ETH Zurich have been considered in this thesis. Two crystals with the $P6_3cm$ symmetry (ErMnO_3 and InMnO_3) and InMnO_3 with the $P\bar{3}c1$ symmetry. Fig. 1.16 shows the three single crystals whose characteristics are reported in Tab. 1.2.



Figure 1.16: (a) ErMnO_3 ($P6_3cm$) (b) InMnO_3 ($P\bar{3}c1$) and (c) InMnO_3 ($P6_3cm$)

	Fig. 1.16(a)	Fig. 1.16(b)	Fig. 1.16(c)
Name	ErMnO_3	$\text{InMnO}_3\# 5$	$\text{InMnO}_3\# 10$
Size	$200 [\mu m] \times 100 [\mu m]$	$50 [\mu m] \times 50 [\mu m]$	$50 [\mu m] \times 50 [\mu m]$
Electric property	FE	PUA	FE

Table 1.2: Parameters of the hexagonal manganite single crystals

The size of the samples induces some experimental difficulties. In infrared spectroscopy, the size of a sample sets a lower limit to the accessible frequency of the measurement due to the diffraction limit. Indeed, the diameter of the first Airy disk is proportional to approximately 3 times the wavelength. Consequently, the reflectivity of a sample of $50 \mu m$ cannot be measured below 200 cm^{-1} . Given the size of the samples and the frequencies of the Higgs modes, an analysis by infrared spectroscopy is not possible. On the other hand, Raman spectroscopy seems to be the best alternative in order to find the Higgs modes.

1.3.4 Raman spectroscopy

Two polarization configurations have been used to control the extinction of the A_1 modes in the $P6_3cm$ symmetry. The parallel configuration is described with the Porto notation as $z, (x, x)\bar{z}$ while the perpendicular one is $z(x, y)\bar{z}$. The z axis describes the direction of the beam perpendicular to the samples surface, while the parallel and perpendicular axis are determined by the well-known extinction of the 514 cm^{-1} phonon peaks in Si.

Fig. 1.17 shows the Raman spectroscopy of ErMnO_3 single crystal at room temperature for the two configurations of the polarized beam. It is observed that the

Raman scattering pattern is in good agreement with the literature [33]. Moreover, the measurement done in cross polarization configuration $z(x, y)\bar{z}$ allows to confirm the predicted polarization selection rule for $P6_3cm$ space group with the extinction of the A_1 modes.

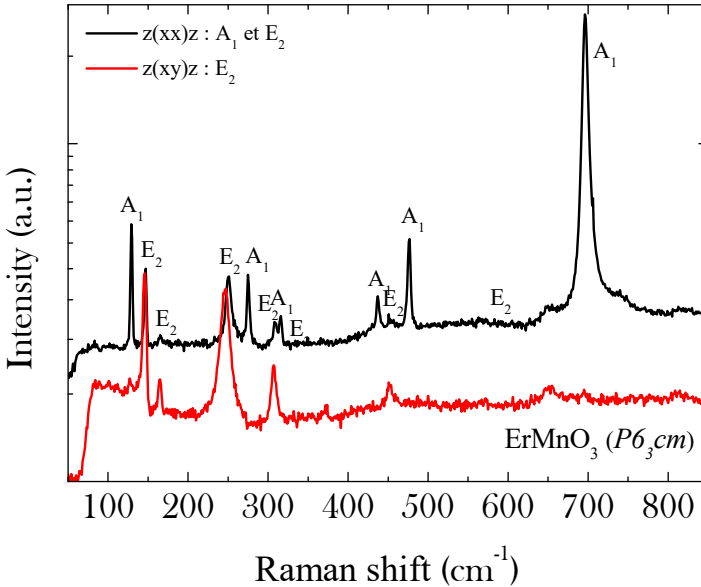


Figure 1.17: Polarization selection rule for the $P6_3cm$ symmetry. Black line, respectively red line, represents the intensity of Raman scattering of ErMnO_3 sample in the parallel configuration, respectively perpendicular configuration.

The polarized Raman spectroscopy performed with two configurations allows to conclude that the single crystal of ErMnO_3 is satisfactory of good quality. Indeed, all the expected Raman active modes are present with sharp shapes.

Raman spectroscopy has been performed on the three samples in a range between 50 and 850 cm^{-1} . Each sample has been measured from 4 K to 350 K in steps of 10/20/25 K. Fig. 1.18 (a), respectively (b) and (c), presents the intensity of the Raman scattering as a function of the Raman shift for the ferroelectric single crystal of ErMnO_3 , respectively for the PUA and ferroelectric single crystal of InMnO_3 . For sake of visibility, the curves have been shifted on the vertical axis proportionally to their temperatures, darker lines representing the lower temperature.

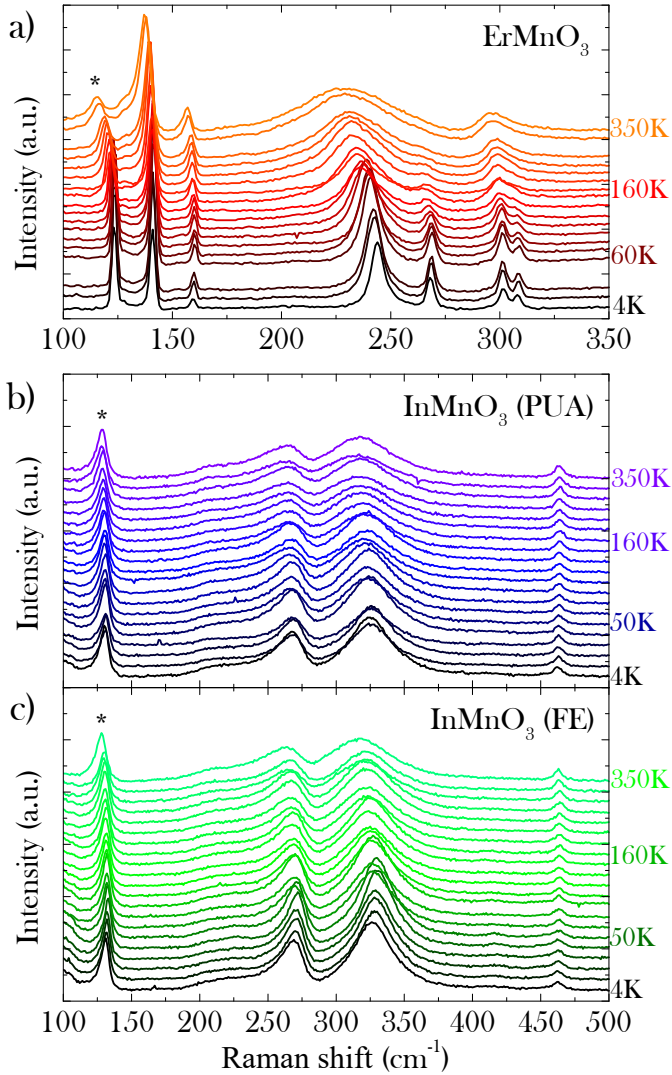


Figure 1.18: Raman shift spectrum as a function of temperature from 4 K to 300 K in steps of 10/20/25 K. (a) ErMnO_3 , (b) InMnO_3 (PUA) and (c) InMnO_3 (FE)

The star on each plot determines the candidates to the being Higgs modes according to the theoretical predictions. No differences between the two InMnO_3 are observed, which means that the two different crystal symmetries are very similar. The positions of the Higgs mode candidates are studied as a function of their shift in temperature. The frequencies of the modes could have been determined by fitting the curves, but the asymmetries of the peaks prevents to obtain reasonable fits by Lorentzian function. Those asymmetries are related to the low intensity of the Raman scattering of the sample due their small sizes and also to their crystalline qualities. In this case, the simplest way to determine the frequency associated to the mode is to consider the maximum.

The relative mode position is defined, for each temperature, as the frequency of the Higgs mode candidate divided by its frequency at 4K. Fig. 1.19 shows the relative mode position as a function of temperature for the three samples. The red line corresponds to the ErMnO_3 sample, the blue line to the InMnO_3 (PUA) and the green line to the InMnO_3 (FE).

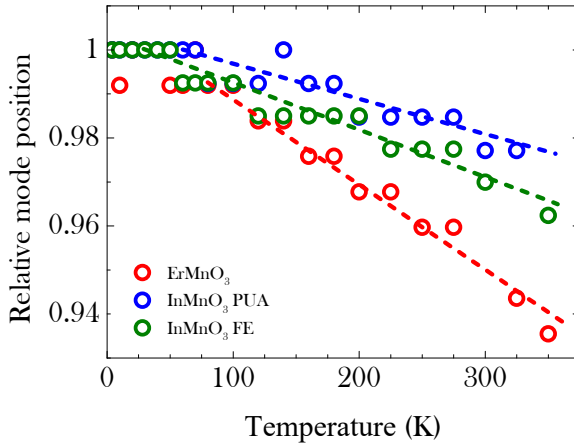


Figure 1.19: Relative phonon position as a function of temperature. The red line corresponds to the ErMnO_3 sample, the blue line to the InMnO_3 (PUA) and the green line to the InMnO_3 (FE). The three arrows act as guidelines for the general behaviors.

A clear shift of 6% is observed for the considered phonon of the ErMnO_3 sample between low and room temperature. The shift is estimated to approximately 4% for the ferroelectric InMnO_3 and to 4% for the partially undistorted anti-polar InMnO_3 .

1.4 Discussion

The frequency shift of the Raman active mode as a function of temperature is a way to probe the harmonicity of the free-energy surface. In a completely harmonic free-energy surface (perfect Mexican hat surface), the Raman spectroscopy, at $T = 0$, probes the excitations between the ground energy state to a higher energy level leading to sharp peaks in the Raman spectra. By increasing the temperature, the measurement probes the higher energy excitations and this leads to the broadening of the peaks. In this kind of harmonic free-energy surface, the peaks get larger but do not shift as a function of temperature. When the free-energy surface is anharmonic, the measurements at $T > 0$ access to energy states out of the harmonic regime and the peaks shift in frequency as a function of the temperature. The shape of the free-energy surface of each sample is different, leading to different levels of anharmonicity. The different levels of anharmonicity are observed between the three different candidates of the Higgs mode but it is also interesting to specify that other modes present an anharmonicity. Indeed, the mode at 250 cm^{-1} in the ErMnO_3 sample is strongly anharmonic. This behavior is then a concrete starting point for a reconsideration of the predicted frequency given by the theoretical calculation.

The relative phonon positions of the three samples present three different shifts as a function of temperature. This behavior was expected. Indeed, these shifts are due to the coupling between the Goldstone and the Higgs modes. In a perfect Mexican hat, the two modes are not coupled and the phonon frequency is not expected to shift as a function of temperature. In the case of a non-perfect Mexican hat shape with "pockets", the coupling between the two modes increases as a function of the depth of the "pockets". Thus, the deeper the pockets are, the stronger is the shift. The non-ferroelectric indium sample (PUA) shows a free-energy surface flatter than the ferroelectric indium sample. Thus, the fact that the shift is stronger for the ferroelectric sample is an important argument. Moreover, the erbium manganate sample presents the deepest pockets in the free-energy surface and the shift of the phonon frequency as a function of temperature is coherently much stronger than the two indium samples.

On the other hand, the estimation of the zero point fluctuation needs to be considered. Indeed, the magnitude of the zero point fluctuation could be higher than the depth of the six pocket holes in the rim of the free-energy surface. If this is the case, the lattice coordinate is completely delocalized along the rim of the hat and coupling between Higgs and Goldstone modes needs to be taken into account.

Additional measurements have to be performed with a high resolution in the low frequencies in order to improve the quality of the spectrum and to refine the frequencies of the candidates. Actually, even if the obtained results are very good and even better than those any other optical studies performed on ErMnO_3 and on InMnO_3 ever published, the shifts of the modes need to be analyzed with more precision in order to determine the accurate behaviors of each sample. Indeed, the estimations of

the shifts are too rough to allow any firm conclusions but show nevertheless a good indication in favor of the association between the candidate modes and the Higgs modes. The growth of larger samples would allow to perform infrared reflectivity and would give complementary information on the candidates of the Higgs mode.

1.5 Conclusion

The Raman spectroscopy performed on the three samples shows some good quality spectra, possibly better than any published data of this type. Indeed, the Raman scattering patterns of each samples has a high signal to noise ratio leading to a good precision of the peaks positions for the ErMnO_3 , as well as for the two InMnO_3 .

According to the theoretical predictions, one Raman active mode per sample has been considered as being a candidate for the Higgs mode. Furthermore, the fact that the shifts of the modes behave as expected is a good indication that these phonons could be Higgs modes.

- [P1] A. Stucky, A. Ubaldini, J. Levallois, M. K. Tran, D. van der Marel and E. Giannini, *Shining light on CuO for exploring high-Tc multiferroics*, *J. Phys. Conf. Series* **566**, 012012 (2014).
- [P2] J. Teyssier, E. Giannini, A. Stucky, R. Cerny, M. V. Eremin and D. van der Marel, *Jahn-Teller induced nematic orbital order in tetragonal Sr₂VO₄*, *Phys. Rev. B* **93**, 125138 (2016).
- [P3] A. Stucky, G. Scheerer, Z. Ren, D. Jaccard, J.-M. Poumirol, C. Barreteau, E. Giannini and D. van der Marel, *Isotope effect in superconducting n-doped SrTiO₃*, *accepted in Scientific Reports* (2016).

References

- [1] ATLAS-Collaboration, *Phys. Lett. B* **716**, 1 (2012).
- [2] J. Ellis, “What is the higgs boson,” CERN Document Server (2012).
- [3] J. Goldstone, A. Salam, and S. Weinberg, *Phys. Rev.* **127**, 965 (1962).
- [4] UA1-Collaboration, *Phys. Lett. B* **126**, 398 (1983).
- [5] UA2-Collaboration, *Phys. Lett. B* **122**, 476 (1983).
- [6] P. D. Group (Particle Data Group), *Phys. Rev. D* **86**, 010001 (2012).
- [7] Y. Nambu, *Phys. Rev.* **117**, 648 (1960).
- [8] P. W. Anderson, *Phys. Rev.* **130**, 439 (1963).
- [9] P. W. Higgs, *Phys. Rev. Lett.* **13**, 508 (1964).
- [10] F. Englert and R. Brout, *Phys. Rev. Lett.* **13**, 321 (1964).
- [11] G. S. Guralnik, C. R. Hagen, and T. W. B. Kibble, *Phys. Rev. Lett.* **13**, 585 (1964).
- [12] J. Goldstone, *Il Nuovo Cimento* **19**, 154 (1961).
- [13] D. Pekker and C. Varma, *Annu. Rev. Cond. Matt. Phys.* **6**, 269 (2015).
- [14] C. Rüegg *et al.*, *Phys. Rev. Lett.* **100**, 205701 (2008).
- [15] M. Matsumoto, B. Normand, T. M. Rice, and M. Sigrist, *Phys. Rev. B* **69**, 054423 (2004).

- [16] C. Rüegg *et al.*, *Phys. Rev. Lett.* **93**, 257201 (2004).
- [17] H. L. Yakel, Jr, W. C. Koehler, E. F. Bertaut, and E. F. Forrat, *Acta Crystallogr.* **16**, 957 (1963).
- [18] B. Lorenz, *ISRN Condensed Matter Physics* **2013**, 43 (2013).
- [19] W. Koehler, H. Yakel, E. Wollan, and J. Cable, *Phys. Lett.* **9**, 93 (1964).
- [20] J. Greedan, M. Bieringer, J. Britten, D. Giaquinta, and H.-C. zur Loye, *J. Solid State Chem.* **116**, 118 (1995).
- [21] F. Yen *et al.*, *J. Mater. Res* **22**, 2163 (2007).
- [22] E. Bertaut and M. Mercier, *Phys. Lett.* **5**, 27 (1963).
- [23] B. Van Aken, T. Palstra, A. Filippetti, and N. A. Spaldin, *Nat. Mater.* **3**, 164 (2004).
- [24] Y. Kumagai *et al.*, *Phys. Rev. B* **85**, 174422 (2012).
- [25] F.-T. Huang *et al.*, *Phys. Rev. B* **87**, 184109 (2013).
- [26] T. Choi *et al.*, *Nat. Mater.* **9**, 253 (2010).
- [27] M. Fiebig, T. Lottermoser, D. Fröhlich, A. Goltsev, and R. Pisarev, *Nature* **419**, 818 (2002).
- [28] S. Artyukhin, K. Delaney, N. Spaldin, and M. Mostovoy, *Nat. Mater.* **13**, 42 (2014).
- [29] S. M. Griffin *et al.*, *Phys. Rev. X* **2**, 041022 (2012).
- [30] F.-T. o. Huang, *Phys. Rev. Lett.* **113**, 267602 (2014).
- [31] D. L. Rousseau, R. P. Bauman, and S. P. S. Porto, *J. Raman Spectrosc.* **10**, 253 (1981).
- [32] M. N. Iliev *et al.*, *Phys. Rev. B* **56**, 2488 (1997).
- [33] J. Vermette, S. Jandl, and M. M. Gospodinov, *J. Phys. Condens. Matt.* **20**, 425219 (2008).
- [34] M. F. Bekheet *et al.*, *J. Solid State Chem.* **241**, 54 (2016).
- [35] Q. Meier and N. A. Spaldin, Private conversation (2016).
- [36] A. Stucky, A. Ubaldini, J. Levallois, M. K. Tran, D. van der Marel, and E. Giannini, *J. Phys. Conf. Serie.* **566**, 012012 (2014).

- [37] J. Teyssier, E. Giannini, A. Stucky, R. Cerny, M. V. Eremin, and D. van der Marel, *Phys. Rev. B* **93**, 125138 (2016).
- [38] A. Stucky, G. Scheerer, Z. Ren, D. Jaccard, J.-M. Poumirol, C. Barreteau, E. Giannini, and D. van der Marel, ArXiv e-prints **1610.10045**, 1 (2016), [arXiv:1610.10045 \[cond-mat.supr-con\]](https://arxiv.org/abs/1610.10045) .